NMR in Biomedicine

Diffusion kurtosis imaging for characterizing tumor heterogeneity in an intracranial rat glioblastoma model

Journal:	*NMR in Biomedicine*
Manuscript ID	NBM-19-0236.R3
Wiley - Manuscript type:	Research Article
Date Submitted by the Author:	n/a
Complete List of Authors:	lesbats, clementine; University of Liverpool, Cellular and Molecular Physiology Kelly, Claire; University of Liverpool, Cellular and Molecular Physiology Czanner, Gabriela; University of Liverpool, Biostatistics; Liverpool John Moores University - City Campus, Experimental Mathematics Poptani, Harish; University of Liverpool, Cellular and Molecular Physiology
Keywords:	Animal model study < Cancer < Applications, Diffusion MR sequences < Diffusion Methods < Methods and Engineering, Diffusion tensor imaging (DTI) < Diffusion Methods < Methods and Engineering

Diffusion kurtosis imaging for characterizing tumor heterogeneity in an intracranial rat glioblastoma model

Clémentine Lesbats[1] PhD, Claire Louise Kelly[1] MRes, Gabriela Czanner[2] PhD, Harish Poptani[1*] PhD

[1]Centre for Preclinical Imaging, Institute of Translational Medicine, University of Liverpool, Liverpool, and [2]Department of Applied Mathematics, Liverpool John Moores University, Liverpool, United Kingdom

*Corresponding author:

Harish Poptani

Centre for Preclinical Imaging, Institute for Translational Medicine

University of Liverpool

Crown Street, L69 3BX, Liverpool

United Kingdom

Phone: +44 1517945444

Email: harish.poptani@liverpool.ac.uk

Word count: 3958

Abbreviations: GBM, Glioblastoma multiforme; DTI, Diffusion Tensor Imaging; DKI, Diffusion Kurtosis Imaging; EPI, Echo Planar Imaging; FA, Fractional Anisotropy; KFA, Kurtosis Fractional Anisotropy; MD, Mean Diffusivity; AD, Axial Diffusivity; RD, Radial

Diffusivity; MK, Mean Kurtosis; AK, Axial Kurtosis; RK, Radial Kurtosis; VOI, Volume Of Interest.

Diffusion kurtosis imaging for characterizing tumor heterogeneity in an intracranial rat glioblastoma model

Abstract:

The utility of diffusion kurtosis imaging (DKI) for assessing intra-tumor heterogeneity was evaluated in a rat model of glioblastoma multiforme.

Longitudinal MRI including T_2-weighted and diffusion weighted MRI (DWI) was performed on six female Fischer rats 8, 11 and 14 days after intracranial transplantation of F98 cells. T_2-weighted images were used to measure the tumor volumes and DWI images were used to compute diffusion tensor imaging (DTI) and DWI parametric maps including mean diffusivity (MD), mean kurtosis (MK), axial diffusivity (AD), axial kurtosis (AK), radial diffusivity (RD), radial kurtosis (RK), fractional anisotropy (FA) and kurtosis fractional anisotropy (KFA). Median values from the segmented normal contralateral cortex, tumor and edema from the diffusion parameters were compared at the three imaging points and computed to assess any changes in tumor heterogeneity over time. *Ex vivo* DKI was also performed in a representative sample and compared with histology.

Significant differences were observed between the normal cortex, tumor and edema in both the DTI and DKI parameters. Notably, at the earliest time point MK and KFA were significantly different between the normal cortex and tumor in comparison to MD or FA. Although a decreasing trend in MD, AD and FA values of the tumor were observed as the tumor grew, no significant changes in any of the DTI or DKI parameters were observed longitudinally.

While DKI was equally sensitive to DTI in differentiating tumor from edema and normal brain, it was unable to detect longitudinal increase of intra-tumoral heterogeneity in the F98 model of glioblastoma multiforme.

Keywords: MRI - diffusion kurtosis imaging; MRI – rat brain tumor; brain tumor; tumor heterogeneity.

Introduction

Glioblastoma multiforme (GBM) is the most frequently occurring central nervous system primary brain tumor with poor prognosis and a median survival rate of 15 months after diagnosis [1]. Of the several rodent models of GBM, the rat orthotopic F98 model has been reported to exhibit several traits of the human GBM in rats [2], including a high degree of heterogeneity, invasiveness and diffused boundaries [3]. It has been used to assess chemo [4,5] and radiation [6] therapy and has also been used in MR studies including spectroscopy [7], diffusion [8-10], and perfusion MRI [6,11].

Diffusion-weighted magnetic resonance imaging (DWI) has been widely used to quantify the random motion of water molecules in biological tissues [12-14]. Standard analytical models processing diffusion-weighted MRI data for computation of the apparent diffusion coefficient (ADC) values assume water displacement in the tissue (voxel of interest) follows a Gaussian statistical distribution, similar to the water diffusion observed in homogeneous liquids. However, it is well known that the assumption of Gaussian distribution fails in *in vivo* conditions due to the inherent heterogeneity from the presence of various tissue compartments, including different cell types, cell morphologies, extracellular matrix, and blood [15].

Diffusion Kurtosis Imaging (DKI) is a dimensionless metric that quantifies how much the water diffusion deviates from a Gaussian distribution due to cellular membranes, intra- and extracellular compartments and tissue structure [15-17]. Thus, the diffusion of water molecules in homogeneous liquids will follow a Gaussian distribution with a kurtosis of zero. In tissues where diffusion is mostly hindered and restricted, water

molecules will more likely diffuse short distances around the initial position in a time *t*, leading to a sharper statistical distribution and a positive kurtosis.

DKI has been used to assess white matter damage and myelin density [17]. Preclinical DKI studies include infarct [18], traumatic brain injury [19] and Alzheimer's disease [20], type 2 diabetic ischemic stroke [21], and acute alcohol intoxication [22].

DKI has also been reported to aid in assessing microstructural heterogeneity in tumors and its degree of diffusion restriction. It has been used in grading of human gliomas whereby higher mean kurtosis (MK) and lower mean diffusivity (MD) values were noted in high-grade solid tumors with increased cellularity [23]. Increased cellularity and presence of spindle-shaped cells led to a higher kurtosis and lower diffusivity in colorectal tumors xenografts [24].

Although promising, none of published studies have assessed longitudinal changes in kurtosis parameters of the tumor for assessing changes in tumor tissue heterogeneity with regards to the microenvironment and cellular components as the tumor grows. Therefore, we performed a longitudinal study in a rat F98 brain tumor model to assess whether changes in DKI parameters can better assess tumor heterogeneity as the tumor volume increases over time.

Methods

Cell culture

F98 glioma cells (ATCC CRL-2937^{TM}), were maintained as adherent monolayers cultured in Dulbecco Modified Eagles Medium containing 4.5 g/L glucose (DMEM D6429, Sigma-Aldrich, St. Louis, Missouri, USA) supplemented with 10% fetal bovine

serum (FBS 10270-106, Gibco, Thermo Fisher Scientific, Waltham, Massachusetts, USA). The cells were maintained at 37 °C in 5% CO_2 humidified atmosphere. Cells were passaged twice weekly at $1x10^5$ per T-75 flask and terminated after the fifth passage to avoid chances of further mutations. Cells were tested bi-monthly for mycoplasma.

Brain tumor model

In vivo studies on rats were conducted in compliance with the UK Home Office Animals (Scientific Procedures) Act 1986 and with the ethical approval of the local committee of the University of Liverpool. Six F344 female (100-120 g) Fischer rats (Charles River, Margate, United Kingdom) were injected with 50,000 F98 cells suspended in 5 µL serum-free DMEM culture medium. The injection was performed in an aseptic environment using sterile tools. The rat was maintained under surgical anesthesia using a 3% isoflurane in O_2 gas mixture. Rats were given subcutaneous injections of antibiotics (5 mg/kg, 25 mg/mL enrofloxacin, 2.5% Baytril, Bayer, Leverkusen, Germany) and analgesia (0.3 mg/mL buprenophine, Vetergesic, Ceva Animal Health, Amersham, UK) before the surgery, and 2 mL saline after the surgery. The rat was maintained in a three-point stereotaxic frame, the head was shaved and a small incision allowed access to the skull. A burr hole was drilled through the skull 3 mm right and 3 mm posterior from the bregma and the cells were injected 2.5 mm deep into the cerebral cortex. After the surgery, the skin was sutured, and the animal was returned to its cage for recovery. Three animals were housed together in a cage with stimulation objects and free access to food and water, which was provided *ad libitum* and the animals were kept in a 12-hour day/light cycle.

MRI acquisition

MRI scans were performed at 9.4 T on a Bruker Biospec (Bruker BioSpin, Ettlingen, Germany). Signal was generated using a 86 mm transmission birdcage coil, and detected by a four-channel phased array surface coil. The rats were anesthetized with 2% isoflurane in O_2 and the respiration rate and body temperature were monitored using an abdominal motion sensor and a rectal probe (SA Instruments, Inc., Stony Brook, New York, USA). The body temperature was maintained at 35 °C by a hot water blanket and the respiration rate at 50-60 inspirations per minute. Each MRI experiment consisted of a localizer scan, followed by an anatomical T_2-weighted sequence and a DWI sequence.

In vivo MR images were acquired longitudinally on days 8, 11 and 14 post- tumor cells inoculation to assess changes in the tumor microenvironment with DKI using a minimum of three time points (early, mid and late tumor stage). These time points were also chosen to comply with the home office guidelines of not subjecting the animal to undue stress of multiple anaesthesia sessions or exceeding the severity limits on animal health. A multi-slice T_2-weighted sequence was acquired to locate the tumor using a fast spin echo sequence with the following parameters: TE/TR = 33/5000 ms, RARE factor = 8, matrix = 256x256, FOV = 40x20 mm, 38 slices, scan duration = 2 min 38 s. DKI was performed using a respiratory-gated EPI-DTI sequence with the parameters: TE/TR = 23/2500 ms, 5 averages, 4 EPI segments, matrix = 128x64, FOV = 40x20 mm, 38 slices, voxel resolution = 0.3x0.3x0.3 mm^3, δ/Δ=4/11 ms, 15 directions, b-values = 0-1000-2000 s/mm^2, 3 b0 images, 27.5 min. The total scan duration for each experiment was around 60 min. Animals were rehydrated with 1 mL saline injected subcutaneously after each MRI session.

Image processing and statistical analysis

The brain was manually segmented on the b = 0 s/mm^2 images from the diffusion-weighted datasets using ITK-SNAP (www.itksnap.org). Tumors were manually segmented on the T_2-weighted images to assess tumoral growth. Tumor growth rate was calculated from the logarithm of the volume ratio from day 8 to day 14, and volumetric doubling-time was then calculated using the exponential growth model [25]. Diffusion and kurtosis parametric maps were calculated using the DKE software (Medical University of South Carolina, USA). A characteristic T_2-weighted image of a typical rat 11 days after tumor cells injection and its corresponding parametric maps are shown in Figure 1. No corrections were made for geometric distortions or eddy current effects. Volumes of interests (VOI) corresponding to the whole tumor, the whole peritumoral edema and the contralateral normal appearing healthy brain parenchyma cortex were also segmented using ITK-SNAP and the binary masks were overlaid on the parametric maps. The contralateral normal brain healthy cortex VOI was segmented by selecting a region of frontal left cortex for every slice containing glioma. As the contralateral normal brain microstructure is unlikely to change due to the presence of the tumor on the ipsi-lateral side, it was used as reference with the hypothesis that no significant changes in the normal brain will be observed while changes in tumor heterogeneity will lead to changes in DKI parameters. Care was taken to keep the normal brain VOI to be as big and as close as possible to the first imaging time point in each animal and during longitudinal studies. Typical VOIs are shown in Figure 2b. Histograms of the parameter value distribution in the tumoral, edematous and cortical regions (Figure 2a and 2c) were generated using MATLAB (Mathworks Inc., Massachusetts, USA). Mean, median and standard deviation values

were calculated for each parameter using Origin (OriginLab, Northampton, Massachusetts, USA). A Wilcoxon signed-rank test was used to compare the tumor diffusion and kurtosis median values to the peritumoral edema and contralateral cortex. A Friedman test was used to compare the longitudinal data. A *p*-value of 0.05 or below was considered to be significantly different between the groups.

Tissue collection

Animals were euthanized one day after the last MRI session using an overdose of 3 mL/kg pentobarbital sodium (Euthatal, Merial Animal Health Ltd, Harlow, UK) injected intra-peritoneally. An incision was performed along the mid-ventral line through the abdomen to severe the aorta under the diaphragm. A midline thoracotomy gave access to the heart. A 25-gauge needle connected to an extension tube was clamped to the left ventricle of the heart to perfuse with 50 mL saline followed by 75 mL 4% Formalin (Sigma-Aldrich, St. Louis, Massachusetts, USA). Following fixation, brains were collected and suspended in 4% Formalin.

***Ex vivo* MRI**

Ex vivo MR images of the brain suspended in perfluoropolyether oil (Fomblin, Solvay, Brussels, Belgium) were acquired using the same T_2-weighted coronal fast spin echo sequence as the *in vivo* protocol except that 25 averages were used (scan duration = 1 h 12 min). DWI was carried out using the same EPI-DTI sequence that was used *in vivo* with 25 averages (scan duration = 3 h 26 min).

Histology

The brain sample that was used for *ex vivo* DKI study, was embedded in paraffin until sectioning after the DKI study. Hematoxylin and eosin (H&E) staining was performed on 4 μm coronal sections across the tumor. The sections closely matching the *ex vivo* imaging slice was qualitatively analyzed and the extent of cell density and cellular organization was based on visual assessment of staining.

Results

Figure 3 shows representative T_2-weighted MR images of a tumor bearing rat brain, in which the developing tumor could be visualized 8, 11 and 14 days after tumor cells inoculation. All six rats developed tumors in the right cortex, visible on the MRI scans from one week post-surgery. The tumor volume grew from 23.63 ± 10.20 mm^3 (day 8) to 112.40 ± 37.77 mm^3 (day 14). Based on these MRI volumetric measurements, the growth rate was 0.116 $days^{-1}$. The tumor volume doubling-time was 3.65 days (n=6) in agreement with other F98 volumetric studies [26-28].

Figure 2 shows the MD and MK histograms in the tumoral, edematous and contralateral regions of a representative rat and their corresponding maps 14 days post-implantation. A higher MD is observed in the tumor compared to the contralateral cortex, but with overlapping distributions (Figure 2a). The peritumoral edema demonstrated higher MD than both the tumor and the contralateral cortex. The highest MK was observed in the tumoral region, whereas the lowest values were found in the edematous region (Figure 2c). However, the MK voxel distributions from the three regions were overlapping.

The median parametric values of the whole tumor excluding the edema, the peritumoral edema and the contralateral cortex volumes of interest (as shown in Figure 2b) for the six rats are shown as scatter plots in Figure 4 and Figure 5 at day 8, 11 and 14. Table 1 provides the mean and standard deviation values of the diffusivity and kurtosis parameters in the six rats.

Tumors were observed on the MD maps with a concentric hyperintense structure composed of the peritumoral edema and the necrotic core (Figure 2b). The tumor appears hyperintense on the MK maps (Figure 2d). The axial (AD) and radial diffusivity (RD) maps showed a concentric structure similar to that observed on the MD maps formed of high diffusivity in the peritumoral edema and necrotic core. Likewise, the axial kurtosis (AK) maps demonstrated hyperintense tumors. On the other hand, the radial kurtosis (RK) maps did not provide a clear definition of the tumor edges.

Tumor vs. contralateral cortex

A Wilcoxon signed-rank test showed a significantly higher MD in the tumor compared to the contralateral cortex from day 11 ($Z = 2.097$, $p = 0.036$) (Figure 4a). Similar to MD, the RD was significantly higher in the tumor than the contralateral cortex as illustrated in Figure 5b. No significant difference was observed between the tumor AD and the contralateral values (Figure 5a). The fractional anisotropy (FA) was significantly lower in the tumor on day 14 (Figure 5c).

The MK was significantly higher in the tumor compared to the contralateral cortex ($Z = 2.097$, $p = 0.036$ for all time points) (Figure 4b). Median RK was also significantly higher in the tumor compared to the contralateral cortex on day 8 and day 11 (Figure 5e), whereas the tumor AK was not significantly different (Figure 5d). Kurtosis

fractional anisotropy (KFA) was significantly lower in the tumor compared to the contralateral cortex at all time points (Figure 5f).

Tumor vs. peritumoral edema

MD was significantly higher in the edema compared to the tumor and the contralateral cortex from day 8 ($Z = 2.097$, $p = 0.036$) (Figure 4a). RD was also significantly higher in the edema compared to the tumor (Figure 5b), and AD was significantly higher only on day 14 (Figure 5a). FA was significantly greater in the edema compared to the tumor (Figure 5c). MK was significantly lower in the edema compared to the tumor ($Z = 2.097$, $p = 0.036$) (Figure 4b). Significant differences were observed for AK at all time points (Figure 4d), and RK at day 8 and day 11 (Figure 5e). KFA did not show any significant difference between the tumor and the peritumoral edema (Figure 5f).

Longitudinal changes in imaging parameters

The Friedman test showed no significant changes in tumor MD ($\chi^2 = 3,\ df = 2,\ p = 0.22$) or MK ($\chi^2 = 1.33,\ df = 2,\ p = 0.51$) values with time as tumor growth occurred. None of the other diffusivity and kurtosis parameters displayed any significant change with time and tumor growth.

***Ex vivo* diffusivity and kurtosis**

Ex vivo MRI scans and corresponding H&E slices of a representative brain are shown in Figure 6. A reduced FA was observed in the necrotic center of the tumor and in the tumor surroundings (Figure 6a, Table 1). KFA followed the same trend (Figure 6b, Table 1). Comparing the histological section with the similar slice section on MRI, demonstrated a dense tumor (visual appearance of higher staining reflecting

increased cell density) on H&E staining (Figure 6f). The necrotic center was hollow due to the fixation and dehydration processes. The tumor edge seemed to have elevated cellular density compared to the contralateral cortex (Figure 6e).

Discussion

In this study, we investigated the utility of diffusion kurtosis to probe intra-tumoral heterogeneity in a rat model of intracranial glioblastoma. Although diffusion kurtosis demonstrated significant difference between the tumor, the peritumoral edema and the contralateral cortex from the early stage, none of the parameters significantly changed as the tumor grew.

We observed an increased mean diffusivity (MD) and mean kurtosis (MK) in the tumor in comparison with the contralateral cortex. The increased MD may be due to increased extracellular diffusivity, or a significant increase in intracellular water diffusion due to cellular swelling. An increased mean diffusivity in tumors relative to the contralateral cortex has been reported in rats with F98 and C6 glioma [8-10,29], although some discrepancy exists since another study reported decreased MD in C6 gliomas [30]. MRI diffusion parameters, such as MD and FA, have shown potential for predicting tumor grade [31,32], treatment monitoring and prognosis [33]. The F98 tumors exhibited higher MK values compared to the contralateral cortex, similar to some human studies reporting higher MK in high grade tumors compared to lower grade glioma [23,34]. However, higher MK has also been associated with inflammation and glial activity in rat model of traumatic brain injury [19,35]. Hempel et al. [36] reported that MK was a robust parameter for WHO classification of human gliomas. In fact, the highest MK values were measured in IDH_{WT} glioblastoma described by an increased

cellularity, cellular heterogeneity, hemorrhage, necrosis and microvasculature proliferation, and the lowest MK values were observed in IDH_{mut} because of their low cell density and homogeneity [37]. The high MK observed in the F98 glioma in our study might originate from the high cellular density of the tumoral rim and the heterogeneity of the necrotic core, which was verified by H&E staining whereby very high cell density was observed in the tumor, and a slightly increased cell density was observed in the peritumoral area compared to the contralateral cortex.

Radial and axial diffusivities (RD and AD) exhibited the same trend as the MD values in the tumor and the contralateral cortex. Previous studies also reported higher RD in F98, 9L and GBM22 rat tumors [8,10]. We observed that RK was higher in the tumor compared to the contralateral cortex on day 8 and 11 whereas AK was not significantly different between the tumor and the normal brain.

A lower FA value was observed in the tumor compared to the normal brain in our study suggesting a more chaotic cellular organization in the tumor. In an earlier study, higher FA in tumor rim than the tumor core has been reported in the F98 model [9]. As the tumor size increased, the necrotic core grew to become the major part of the tumor VOI by day 14 thereby contributing predominantly to the whole tumor diffusion anisotropy measurements in our study. Similar to our observations, increases in FA have been reported in human tumors from grade II to IV gliomas [31]. Lower KFA from the F98 tumor, especially from the necrotic center indicates a much lower degree of tissue organization. KFA, which represents the anisotropy of the kurtosis tensor, has been recently proposed as useful microstructural contrast [38,39]. Although this metric is more appropriate for white matter analysis in the case of several crossing fiber

orientations in the same voxel, it also seems to be of interest for grey matter microstructure description as elevated KFA was observed in tissues with low anisotropy such as the thalamus and lenticular nucleus where the cells are organized in oriented structures (e.g. lamina, nuclei) [39]. The variability in the normal brain VOI parameters (Figure 5) was larger than expected, especially in the FA, RK and KFA values. The fact that this variability is not observed in all the parameters, suggests that there might be some variability in the selection of the VOI, leading to different GM/WM ratios, and that FA, KFA and RK are probably more sensitive to these subtle alterations than the other DTI and DKI parameters. We observed decreased KFA in the tumoral tissue, suggesting a lower degree of overall tissue organization, which was noted in H&E stains showing high cellular density in the tumor with heterogeneity due to the necrotic cores.

The peritumoral edema displayed higher MD due to increased extracellular water. The increased water diffusion in all directions causes a significant decrease in diffusional kurtosis compared to the contralateral cortex, but also relative to the tumor. Furthermore, the peritumoral edema FA was always significantly higher than that of the tumor. An increased peritumoral edema FA and increased MD were also described in several F98 and 9L rat glioma studies [8-10]. However, an increased FA and decreased ADC (MD) in the area surrounding the tumor was reported by Kim et al. [10] and by Lope-Piedrafita et al. in 9L, F98 and C6 rat glioma, assumed to be caused by the compression of the surrounding cells to an oblate spheroid shape [40]. The increased diffusion anisotropy measured in the peritumoral region can be explained by the compression of the grey matter by the tumor mass, but also the infiltration of the tumor in the surrounding tissue. The H&E staining shows a higher cellular density in the

edematous region. Furthermore, the cells seem to be more elongated in the region directly surrounding the tumor than in the contralateral cortex due to a tumoral mass effect, as suggested by Lope-Piedrafita [40]. It seems that our F98 glioma model is not only highly infiltrative but also demonstrates a mass effect on the nearby tissue.

Diffusion kurtosis imaging (DKI) provides dimensionless metrics on the deviation of the probabilistic water displacement from a Gaussian distribution and has been proposed to better characterize tumor heterogeneity than standard DTI parameters in several pathological conditions (24). In contrast to our hypothesis, we did not observe any temporal evolution in DKI parameters with tumor growth, as the tumor tissue clearly became more heterogenous with time, with increased necrotic areas. An increase of ADC over time has been reported by Letourneur et al. [29] in a rat model with C6 glioma. However, no changes of ADC was observed in in F98 tumors [29] or 9L tumors [41].

Our study did not show any better sensitivity in identifying tumor tissue from healthy brain with DKI, compared to DTI at all imaging time points. Our initial hypothesis was that as the tumor grows, the increased microstructural heterogeneity due to hypoxia and necrosis would be quantifiable using DKI parameters. The lack of significant changes may either be due to tumor biology or due to limitations of the DKI technique. Firstly, the DKI data were acquired at 9.4 T using two non-zero b-values that should theoretically allow kurtosis calculation in our model [38,42], but only two b-values may have not provided enough sensitivity in measuring early microstructural changes, as suggested by other reports which used several low and high b-values combinations [15,17]. The use of the b=0 values for both the DTI and DKI analysis led to some contributions from the fast (vascular) components of water diffusion due to the intra

voxel intra molecular (IVIM) effect. However, since the IVIM effect would have impacted both the DTI and DKI measurements, we believe that the IVIM effects would have cancelled out while comparing the two (DTI versus DKI) for assessing tumor tissue heterogeneity. Additionally, although most human DKI studies are performed using 30 diffusion encoding directions, based on the recommendations of the DKE software, we used 15 diffusion directions in our study as the best compromise between SNR and acquisition time. However, we do not believe that the reduced number of diffusion direction impacts on the DKI fitting as it has been reported that DKI parameters can be calculated using a minimum of 15 diffusion directions [15,16]. Preclinical DKI studies have been reported with 15 directions in a rat model of stroke at 4.7T [43], and 20 directions in diabetic rats at 7T [21]. In fact, Latt et al. demonstrated that even 6 directions are sufficient to reach a good estimate of diffusion kurtosis in human MS at 3T [44]. Another probable reason for not observing any change in kurtosis with tumor growth could be that the tumor was already highly heterogeneous (microstructurally) at the earliest imaging time point. In fact, a necrotic core was observed on the anatomical scans and parametric maps in all of the tumors from day 11 post-implantation (second imaging time point). It is possible that the subsequent changes in tumor heterogeneity were not substantial enough to be detected with diffusion kurtosis MRI. The use of complementary imaging techniques could be useful to assess cellular swelling and extracellular matrix alterations such as time-dependent DTI that was used in tumor models to separate the intracellular and extracellular water diffusion [45,46]. Alternatively, a slower growing tumor model could be used, or a treatment paradigm that substantially alters the tissue microstructure by induction of therapeutic cell death.

In conclusion, an increased diffusional kurtosis in F98 tumors, and a decrease in the peritumoral edema was observed compared to the normal brain, although no changes in DKI parameters were noted as the tumor grew, indicating that this technique may not be able to observe the microstructural tumor heterogeneity in the F98 model.

Acknowledgements: Dr Arthur Taylor, University of Liverpool, is acknowledged for providing the F98 cells and the protocol for tumor transplantation. Imaging studies were performed at the Centre for Preclinical Imaging, which was funded in part by a Medical Research Council (MRC) grant (MR/L012707/1).

Figure Legends

Figure 1: Representative T_2-weighted image (a) and its corresponding diffusivity (b) and kurtosis (c) parametric maps. The red arrow indicates the tumor location on the T_2-weighted image.

Figure 2: Mean diffusivity (a) and mean kurtosis (c) histograms in the tumor of a representative rat 14 days after tumor cell injection compared to the contralateral cortex and peritumoral edema and their corresponding mean diffusivity (b) and mean kurtosis (d) maps. The tumor (red), peritumoral edema (green) and contralateral cortex (blue) volumes-of-interest contours are illustrated on the MD (b) and MK (d) maps.

Figure 3: Typical T_2-weighted images of the same rat at a similar slice level showing the presence of F98 tumors (top row, arrow). Boxplots showing the tumor volumes segmented from T_2-weighted images in the six rats 8, 11 and 14 days post-implantation (bottom row).

Figure 4: Comparison boxplots of the median values of mean diffusivity (MD) (a, left) and mean kurtosis (MK) (b, left) in the six rats in the tumor (red), peritumoral edema (yellow) and contralateral cortex (blue) (*: $p<0.05$), and representative MD and MK maps at day 8, day 11 and day 14 (right).

Figure 5: Boxplots of the axial diffusivity (a), radial diffusivity (b), fractional anisotropy (c), axial kurtosis (d), radial kurtosis (e) and kurtosis fractional anisotropy (f) in the

tumor, the contralateral healthy cortex and the edema, day 8, 11 and 14 post-implantation (*: $p<0.05$).

Figure 6: FA (a) and KFA (b) maps of an *ex vivo* rat brain and corresponding 10X H&E staining (c). 20X magnification on the edematous region (d), the tumor edge (e), the tumor center (f) and the contralateral cortex (g). The red arrows indicate the tumor on the FA and KFA maps.

References

1. Hanif F, Muzaffar K, Perveen K, Malhi SM, Simjee SU. Glioblastoma Multiforme: A Review of its Epidemiology and Pathogenesis through Clinical Presentation and Treatment. *Asian Pacific Journal of Cancer Prevention : APJCP.* 2017;18(1):3-9.
2. Barth RF, Kaur B. Rat brain tumor models in experimental neuro-oncology: the C6, 9L, T9, RG2, F98, BT4C, RT-2 and CNS-1 gliomas. *Journal of Neuro-Oncology.* 2009;94(3):299-312.
3. Ortensi B, Setti M, Osti D, Pelicci G. Cancer stem cell contribution to glioblastoma invasiveness. *Stem Cell Research & Therapy.* 2013;4(1):18.
4. Coquery N, Serduc R, Rémy C, Barbier EL, Lemasson B. Cluster versus ROI analysis to assess combined antiangiogenic therapy and radiotherapy in the F98 rat-glioma model. *NMR in Biomedicine.* 2018;31(8):e3933.
5. Côté J, Savard M, Bovenzi V, et al. Selective tumor blood–brain barrier opening with the kinin B2 receptor agonist [Phe8ψ(CH2NH)Arg9]-BK in a F98 glioma rat model: An MRI study. *Neuropeptides.* 2010;44(2):177-185.
6. Bolcaen J, Descamps B, Acou M, et al. In Vivo DCE-MRI for the Discrimination Between Glioblastoma and Radiation Necrosis in Rats. *Molecular Imaging and Biology.* 2017;19(6):857-866.
7. Coquery N, Stupar V, Farion R, et al. The three glioma rat models C6, F98 and RG2 exhibit different metabolic profiles: in vivo 1H MRS and ex vivo 1H HRMAS combined with multivariate statistics. *Metabolomics.* 2015;11(6):1834-1847.
8. Wang S, Zhou J. Diffusion tensor MR imaging of rat glioma models: A correlation study of MR imaging and histology. *Journal of computer assisted tomography.* 2012;36(6):739-744.

9. Zhang J, van Zijl PCM, Laterra J, et al. Unique Patterns of Diffusion Directionality in Rat Brain Tumors Revealed by High-Resolution Diffusion Tensor MRI. *Magnetic resonance in medicine : official journal of the Society of Magnetic Resonance in Medicine / Society of Magnetic Resonance in Medicine.* 2007;58(3):454-462.

10. Kim S, Pickup S, Hsu O, Poptani H. Diffusion tensor MRI in rat models of invasive and well-demarcated brain tumors. *NMR in Biomedicine.* 2007;21(3):208-216.

11. Engelhorn T, Schwarz MA, Hess A, et al. Definition of Ktrans and FA Thresholds for Better Assessment of Experimental Glioma Using High-field MRI: A Feasibility Study. *Clinical Neuroradiology.* 2014;24(4):337-345.

12. Le Bihan D, Breton E, Lallemand D, Aubin ML, Vignaud J, Laval-Jeantet M. Separation of diffusion and perfusion in intravoxel incoherent motion MR imaging. *Radiology.* 1988;168(2):497-505.

13. Le Bihan D, Breton E, Lallemand D, Grenier P, Cabanis E, Laval-Jeantet M. MR imaging of intravoxel incoherent motions: application to diffusion and perfusion in neurologic disorders. *Radiology.* 1986;161(2):401-407.

14. Stejskal EO, Tanner JE. Spin Diffusion Measurements: Spin Echoes in the Presence of a Time-Dependent Field Gradient. *The Journal of Chemical Physics.* 1965;42(1):288-292.

15. Jensen JH, Helpern JA. MRI quantification of non-Gaussian water diffusion by kurtosis analysis. *NMR in Biomedicine.* 2010;23(7):698-710.

16. Jensen JH, Helpern JA, Ramani A, Lu H, Kaczynski K. Diffusional kurtosis imaging: The quantification of non-gaussian water diffusion by means of

magnetic resonance imaging. *Magnetic Resonance in Medicine.* 2005;53(6):1432-1440.

17. Fieremans E, Jensen JH, Helpern JA. White matter characterization with diffusional kurtosis imaging. *NeuroImage.* 2011;58(1):177-188.

18. Umesh Rudrapatna S, Wieloch T, Beirup K, et al. Can diffusion kurtosis imaging improve the sensitivity and specificity of detecting microstructural alterations in brain tissue chronically after experimental stroke? Comparisons with diffusion tensor imaging and histology. *NeuroImage.* 2014;97:363-373.

19. Braeckman K, Descamps B, Pieters L, Vral A, Caeyenberghs K, Vanhove C. Dynamic changes in hippocampal diffusion and kurtosis metrics following experimental mTBI correlate with glial reactivity. *NeuroImage: Clinical.* 2019;21:101669.

20. Vanhoutte G, Pereson S, Delgado y Palacios R, et al. Diffusion kurtosis imaging to detect amyloidosis in an APP/PS1 mouse model for Alzheimer's disease. *Magnetic Resonance in Medicine.* 2013;69(4):1115-1121.

21. Ding G, Chen J, Chopp M, et al. White matter changes after stroke in type 2 diabetic rats measured by diffusion magnetic resonance imaging. *Journal of Cerebral Blood Flow & Metabolism.* 2015;37(1):241-251.

22. Chen X-r, Zeng J-y, Shen Z-W, Kong L-m, Zheng W-b. Diffusion Kurtosis Imaging Detects Microstructural Changes in the Brain after Acute Alcohol Intoxication in Rats. *BioMed Research International.* 2017;2017:6.

23. Hempel JM, Schittenhelm J, Bisdas S, et al. In vivo assessment of tumor heterogeneity in WHO 2016 glioma grades using diffusion kurtosis imaging: Diagnostic performance and improvement of feasibility in routine clinical practice. *Journal of Neuroradiology.* 2018;45(1):32-40.

24. Liu H, Shen W, Zhang C, et al. Diffusion kurtosis imaging evaluating epithelial–mesenchymal transition in colorectal carcinoma xenografts model: a preliminary study. *Scientific Reports.* 2017;7(1):11424.

25. Talkington A, Durrett R. Estimating Tumor Growth Rates In Vivo. *Bulletin of mathematical biology.* 2015;77(10):1934-1954.

26. Mathieu D, Lecomte R, Tsanaclis AM, Larouche A, Fortin D. Standardization and Detailed Characterization of the Syngeneic Fischer/F98 Glioma Model. *Canadian Journal of Neurological Sciences / Journal Canadien des Sciences Neurologiques.* 2007;34(3):296-306.

27. Doblas S, He T, Saunders D, et al. Glioma morphology and tumor-induced vascular alterations revealed in seven rodent glioma models by in vivo magnetic resonance imaging and angiography. 2010;32(2):267-275.

28. Yang W, Barth RF, Wu G, et al. Development of a Syngeneic Rat Brain Tumor Model Expressing EGFRvIII and Its Use for Molecular Targeting Studies with Monoclonal Antibody L8A4. 2005;11(1):341-350.

29. Letourneur A, Roussel S, Bernaudin M, et al. Chronic arterial hypertension impedes glioma growth: a multiparametric MRI study in the rat. *Hypertension Research.* 2015;38:723.

30. Bennett KM, Hyde JS, Rand SD, et al. Intravoxel distribution of DWI decay rates reveals C6 glioma invasion in rat brain. *Magnetic Resonance in Medicine.* 2004;52(5):994-1004.

31. Inoue T, Ogasawara K, Beppu T, Ogawa A, Kabasawa H. Diffusion tensor imaging for preoperative evaluation of tumor grade in gliomas. *Clinical Neurology and Neurosurgery.* 2005;107(3):174-180.

32. Leu K, Ott GA, Lai A, et al. Perfusion and diffusion MRI signatures in histologic and genetic subtypes of WHO grade II–III diffuse gliomas. *Journal of Neuro-Oncology.* 2017;134(1):177-188.

33. Ellingson BM, Gerstner ER, Smits M, et al. Diffusion MRI Phenotypes Predict Overall Survival Benefit from Anti-VEGF Monotherapy in Recurrent Glioblastoma: Converging Evidence from Phase II Trials. *Clinical Cancer Research.* 2017;23(19):5745.

34. Van Cauter S, Veraart J, Sijbers J, et al. Gliomas: Diffusion Kurtosis MR Imaging in Grading. *Radiology.* 2012;263(2):492-501.

35. Zhuo J, Xu S, Proctor JL, et al. Diffusion kurtosis as an in vivo imaging marker for reactive astrogliosis in traumatic brain injury. *NeuroImage.* 2012;59(1):467-477.

36. Hempel J-M, Schittenhelm J, Brendle C, et al. Histogram analysis of diffusion kurtosis imaging estimates for in vivo assessment of 2016 WHO glioma grades: A cross-sectional observational study. *European Journal of Radiology.* 2017;95:202-211.

37. Hempel J-M, Bisdas S, Schittenhelm J, et al. In vivo molecular profiling of human glioma using diffusion kurtosis imaging. *Journal of Neuro-Oncology.* 2017;131(1):93-101.

38. Hansen B, Jespersen SN. Kurtosis fractional anisotropy, its contrast and estimation by proxy. *Scientific Reports.* 2016;6:23999.

39. Glenn GR, Helpern JA, Tabesh A, Jensen JH. Quantitative assessment of diffusional kurtosis anisotropy. *NMR in Biomedicine.* 2015;28(4):448-459.

40. Lope-Piedrafita S, Garcia-Martin ML, Galons J-P, Gillies RJ, Trouard TP. Longitudinal diffusion tensor imaging in a rat brain glioma model. *NMR in Biomedicine.* 2008;21(8):799-808.

41. Kopelman R, Lee Koo Y-E, Philbert M, et al. Multifunctional nanoparticle platforms for in vivo MRI enhancement and photodynamic therapy of a rat brain cancer. *Journal of Magnetism and Magnetic Materials.* 2005;293(1):404-410.

42. Yan X, Zhou M, Ying L, et al. Evaluation of optimized b-value sampling schemas for diffusion kurtosis imaging with an application to stroke patient data. *Computerized Medical Imaging and Graphics.* 2013;37(4):272-280.

43. Sun PZ, Wang Y, Mandeville E, Chan S-T, Lo EH, Ji X. Validation of fast diffusion kurtosis MRI for imaging acute ischemia in a rodent model of stroke. *NMR in Biomedicine.* 2014;27(11):1413-1418.

44. Lätt J, Nilsson M, Wirestam R, et al. In vivo visualization of displacement-distribution-derived parameters in q-space imaging. *Magnetic Resonance Imaging.* 2008;26(1):77-87.

45. Reynaud O, Winters KV, Hoang DM, Wadghiri YZ, Novikov DS, Kim SG. Surface-to-volume ratio mapping of tumor microstructure using oscillating gradient diffusion weighted imaging. *Magnetic Resonance in Medicine.* 2016;76(1):237-247.

46. Hope TR, White NS, Kuperman J, et al. Demonstration of Non-Gaussian Restricted Diffusion in Tumor Cells Using Diffusion Time-Dependent Diffusion-Weighted Magnetic Resonance Imaging Contrast. *Frontiers in Oncology.* 2016;6(179).

Table 1: Mean ± standard deviation for all diffusion and kurtosis parameters in the tumor, edema and contralateral cortex volumes-of-interest of the six rats. (**#**: significant difference between the tumor and the contralateral cortex, **$**: significant difference between the tumor and the edema). Mean and standard deviation from the *ex vivo* data were taken from the volume of interest in one representative rat.

		MD x 10^{-3} (μm^2/ms)	AD x 10^{-3} (μm^2/ms)	RD x 10^{-3} (μm^2/ms)	FA	MK	AK	RK	KFA
Day 8	**Tumor**	0.78±0.04	0.90±0.06	0.71±0.04	0.16±0.04	0.87±0.05	0.89±0.07	0.86±0.09	0.49±0.15
	Edema	0.87±0.06 **$**	1.03±0.08	0.79±0.06 **$**	0.19±0.02	0.76±0.03 **$**	0.78±0.06 **$**	0.75±0.05 **$**	0.50±0.16
	Contralateral cortex	0.71±0.03	0.84±0.03 **#**	0.64±0.03 **#**	0.17±0.03	0.78±0.09 **#**	0.75±0.26	0.70±0.17 **#**	0.60±0.18 **#**
Day 11	**Tumor**	0.75±0.04	0.86±0.05	0.70±0.03	0.15±0.03	0.84±0.06	0.91±0.79	0.79±0.11	0.47±0.10
	Edema	0.88±0.03 **$**	1.03±0.08	0.79±0.03 **$**	0.22±0.02 **$**	0.74±0.04 **$**	0.79±0.03 **$**	0.71±0.08 **$**	0.50±0.09
	Contralateral cortex	0.68±0.04 **#**	0.78±0.04	0.61±0.04 **#**	0.19±0.05	0.75±0.07 **#**	0.92±0.02	0.67±0.12 **#**	0.62±0.11 **#**
Day 14	**Tumor**	0.74±0.05	0.83±0.03	0.67±0.02	0.14±0.03	0.82±0.08	0.88±0.06	0.77±0.08	0.49±0.06
	Edema	0.89±0.04 **$**	1.07±0.05 **$**	0.80±0.04 **$**	0.22±0.02 **$**	0.73±0.02 **$**	0.74±0.04 **$**	0.72±0.06	0.46±0.06
	Contralateral cortex	0.67±0.01 **#**	0.82±0.03	0.59±0.01 **#**	0.22±0.02 **#**	0.72±0.06 **#**	0.83±0.06	0.73±0.11	0.62±0.05 **#**
Ex vivo	**Tumor**	0.55±0.08	0.63±0.08	0.51±0.08	0.18±0.07	0.90±0.15	0.86±0.14	0.83±0.18	0.42±0.08
	Contralateral cortex	0.31±0.01	0.37±0.02	0.28±0.01	0.23±0.03	1.65±0.12	1.61±0.17	1.56±0.16	0.50±0.05

Diffusion kurtosis imaging for characterizing tumor heterogeneity in an intracranial rat glioblastoma model

Clémentine Lesbats[1] PhD, Claire Louise Kelly[1] MRes, Gabriela Czanner[2] PhD, Harish Poptani[1*] PhD

[1]Centre for Preclinical Imaging, Institute of Translational Medicine, University of Liverpool, Liverpool, and [2]Department of Applied Mathematics, Liverpool John Moores University, Liverpool, United Kingdom

*Corresponding author:

Harish Poptani

Centre for Preclinical Imaging, Institute for Translational Medicine

University of Liverpool

Crown Street, L69 3BX, Liverpool

United Kingdom

Phone: +44 1517945444

Email: harish.poptani@liverpool.ac.uk

Word count: 3958

Abbreviations: GBM, Glioblastoma multiforme; DTI, Diffusion Tensor Imaging; DKI, Diffusion Kurtosis Imaging; EPI, Echo Planar Imaging; FA, Fractional Anisotropy; KFA, Kurtosis Fractional Anisotropy; MD, Mean Diffusivity; AD, Axial Diffusivity; RD, Radial

Diffusivity; MK, Mean Kurtosis; AK, Axial Kurtosis; RK, Radial Kurtosis; VOI, Volume Of Interest.

Diffusion kurtosis imaging for characterizing tumor heterogeneity in an intracranial rat glioblastoma model

Abstract:

The utility of diffusion kurtosis imaging (DKI) for assessing intra-tumor heterogeneity was evaluated in a rat model of glioblastoma multiforme.

Longitudinal MRI including T_2-weighted and diffusion weighted MRI (DWI) was performed on six female Fischer rats 8, 11 and 14 days after intracranial transplantation of F98 cells. T_2-weighted images were used to measure the tumor volumes and DWI images were used to compute diffusion tensor imaging (DTI) and DWI parametric maps including mean diffusivity (MD), mean kurtosis (MK), axial diffusivity (AD), axial kurtosis (AK), radial diffusivity (RD), radial kurtosis (RK), fractional anisotropy (FA) and kurtosis fractional anisotropy (KFA). Median values from the segmented normal contralateral cortex, tumor and edema from the diffusion parameters were compared at the three imaging points and computed to assess any changes in tumor heterogeneity over time. *Ex vivo* DKI was also performed in a representative sample and compared with histology.

Significant differences were observed between the normal cortex, tumor and edema in both the DTI and DKI parameters. Notably, at the earliest time point MK and KFA were significantly different between the normal cortex and tumor in comparison to MD or FA. Although a decreasing trend in MD, AD and FA values of the tumor were observed as the tumor grew, no significant changes in any of the DTI or DKI parameters were observed longitudinally.

While DKI was equally sensitive to DTI in differentiating tumor from edema and normal brain, it was unable to detect longitudinal increase of intra-tumoral heterogeneity in the F98 model of glioblastoma multiforme.

Keywords: MRI - diffusion kurtosis imaging; MRI – rat brain tumor; brain tumor; tumor heterogeneity.

Introduction

Glioblastoma multiforme (GBM) is the most frequently occurring central nervous system primary brain tumor with poor prognosis and a median survival rate of 15 months after diagnosis [1]. Of the several rodent models of GBM, the rat orthotopic F98 model has been reported to exhibit several traits of the human GBM in rats [2], including a high degree of heterogeneity, invasiveness and diffused boundaries [3]. It has been used to assess chemo [4,5] and radiation [6] therapy and has also been used in MR studies including spectroscopy [7], diffusion [8-10], and perfusion MRI [6,11].

Diffusion-weighted magnetic resonance imaging (DWI) has been widely used to quantify the random motion of water molecules in biological tissues [12-14]. Standard analytical models processing diffusion-weighted MRI data for computation of the apparent diffusion coefficient (ADC) values assume water displacement in the tissue (voxel of interest) follows a Gaussian statistical distribution, similar to the water diffusion observed in homogeneous liquids. However, it is well known that the assumption of Gaussian distribution fails in *in vivo* conditions due to the inherent heterogeneity from the presence of various tissue compartments, including different cell types, cell morphologies, extracellular matrix, and blood [15].

Diffusion Kurtosis Imaging (DKI) is a dimensionless metric that quantifies how much the water diffusion deviates from a Gaussian distribution due to cellular membranes, intra- and extracellular compartments and tissue structure [15-17]. Thus, the diffusion of water molecules in homogeneous liquids will follow a Gaussian distribution with a kurtosis of zero. In tissues where diffusion is mostly hindered and restricted, water

molecules will more likely diffuse short distances around the initial position in a time *t*, leading to a sharper statistical distribution and a positive kurtosis.

DKI has been used to assess white matter damage and myelin density [17]. Preclinical DKI studies include infarct [18], traumatic brain injury [19] and Alzheimer's disease [20], type 2 diabetic ischemic stroke [21], and acute alcohol intoxication [22].

DKI has also been reported to aid in assessing microstructural heterogeneity in tumors and its degree of diffusion restriction. It has been used in grading of human gliomas whereby higher mean kurtosis (MK) and lower mean diffusivity (MD) values were noted in high-grade solid tumors with increased cellularity [23]. Increased cellularity and presence of spindle-shaped cells led to a higher kurtosis and lower diffusivity in colorectal tumors xenografts [24].

Although promising, none of published studies have assessed longitudinal changes in kurtosis parameters of the tumor for assessing changes in tumor tissue heterogeneity with regards to the microenvironment and cellular components as the tumor grows. Therefore, we performed a longitudinal study in a rat F98 brain tumor model to assess whether changes in DKI parameters can better assess tumor heterogeneity as the tumor volume increases over time.

Methods

Cell culture

F98 glioma cells (ATCC CRL-2937^{TM}), were maintained as adherent monolayers cultured in Dulbecco Modified Eagles Medium containing 4.5 g/L glucose (DMEM D6429, Sigma-Aldrich, St. Louis, Missouri, USA) supplemented with 10% fetal bovine

serum (FBS 10270-106, Gibco, Thermo Fisher Scientific, Waltham, Massachusetts, USA). The cells were maintained at 37 °C in 5% CO_2 humidified atmosphere. Cells were passaged twice weekly at $1x10^5$ per T-75 flask and terminated after the fifth passage to avoid chances of further mutations. Cells were tested bi-monthly for mycoplasma.

Brain tumor model

In vivo studies on rats were conducted in compliance with the UK Home Office Animals (Scientific Procedures) Act 1986 and with the ethical approval of the local committee of the University of Liverpool. Six F344 female (100-120 g) Fischer rats (Charles River, Margate, United Kingdom) were injected with 50,000 F98 cells suspended in 5 µL serum-free DMEM culture medium. The injection was performed in an aseptic environment using sterile tools. The rat was maintained under surgical anesthesia using a 3% isoflurane in O_2 gas mixture. Rats were given subcutaneous injections of antibiotics (5 mg/kg, 25 mg/mL enrofloxacin, 2.5% Baytril, Bayer, Leverkusen, Germany) and analgesia (0.3 mg/mL buprenophine, Vetergesic, Ceva Animal Health, Amersham, UK) before the surgery, and 2 mL saline after the surgery. The rat was maintained in a three-point stereotaxic frame, the head was shaved and a small incision allowed access to the skull. A burr hole was drilled through the skull 3 mm right and 3 mm posterior from the bregma and the cells were injected 2.5 mm deep into the cerebral cortex. After the surgery, the skin was sutured, and the animal was returned to its cage for recovery. Three animals were housed together in a cage with stimulation objects and free access to food and water, which was provided *ad libitum* and the animals were kept in a 12-hour day/light cycle.

MRI acquisition

MRI scans were performed at 9.4 T on a Bruker Biospec (Bruker BioSpin, Ettlingen, Germany). Signal was generated using a 86 mm transmission birdcage coil, and detected by a four-channel phased array surface coil. The rats were anesthetized with 2% isoflurane in O_2 and the respiration rate and body temperature were monitored using an abdominal motion sensor and a rectal probe (SA Instruments, Inc., Stony Brook, New York, USA). The body temperature was maintained at 35 °C by a hot water blanket and the respiration rate at 50-60 inspirations per minute. Each MRI experiment consisted of a localizer scan, followed by an anatomical T_2-weighted sequence and a DWI sequence.

In vivo MR images were acquired longitudinally on days 8, 11 and 14 post- tumor cells inoculation to assess changes in the tumor microenvironment with DKI using a minimum of three time points (early, mid and late tumor stage). These time points were also chosen to comply with the home office guidelines of not subjecting the animal to undue stress of multiple anaesthesia sessions or exceeding the severity limits on animal health. A multi-slice T_2-weighted sequence was acquired to locate the tumor using a fast spin echo sequence with the following parameters: TE/TR = 33/5000 ms, RARE factor = 8, matrix = 256x256, FOV = 40x20 mm, 38 slices, scan duration = 2 min 38 s. DKI was performed using a respiratory-gated EPI-DTI sequence with the parameters: TE/TR = 23/2500 ms, 5 averages, 4 EPI segments, matrix = 128x64, FOV = 40x20 mm, 38 slices, voxel resolution = 0.3x0.3x0.3 mm^3, δ/Δ=4/11 ms, 15 directions, b-values = 0-1000-2000 s/mm^2, 3 b0 images, 27.5 min. The total scan duration for each experiment was around 60 min. Animals were rehydrated with 1 mL saline injected subcutaneously after each MRI session.

Image processing and statistical analysis

The brain was manually segmented on the b = 0 s/mm^2 images from the diffusion-weighted datasets using ITK-SNAP (www.itksnap.org). Tumors were manually segmented on the T_2-weighted images to assess tumoral growth. Tumor growth rate was calculated from the logarithm of the volume ratio from day 8 to day 14, and volumetric doubling-time was then calculated using the exponential growth model [25]. Diffusion and kurtosis parametric maps were calculated using the DKE software (Medical University of South Carolina, USA). A characteristic T_2-weighted image of a typical rat 11 days after tumor cells injection and its corresponding parametric maps are shown in Figure 1. No corrections were made for geometric distortions or eddy current effects. Volumes of interests (VOI) corresponding to the whole tumor, the whole peritumoral edema and the contralateral normal appearing healthy brain parenchyma cortex were also segmented using ITK-SNAP and the binary masks were overlaid on the parametric maps. The contralateral normal brain healthy cortex VOI was segmented by selecting a region of frontal left cortex for every slice containing glioma. As the contralateral normal brain microstructure is unlikely to change due to the presence of the tumor on the ipsi-lateral side, it was used as reference with the hypothesis that no significant changes in the normal brain will be observed while changes in tumor heterogeneity will lead to changes in DKI parameters. Care was taken to keep the normal brain VOI to be as big and as close as possible to the first imaging time point in each animal and during longitudinal studies. Typical VOIs are shown in Figure 2b. Histograms of the parameter value distribution in the tumoral, edematous and cortical regions (Figure 2a and 2c) were generated using MATLAB (Mathworks Inc., Massachusetts, USA). Mean, median and standard deviation values

were calculated for each parameter using Origin (OriginLab, Northampton, Massachusetts, USA). A Wilcoxon signed-rank test was used to compare the tumor diffusion and kurtosis median values to the peritumoral edema and contralateral cortex. A Friedman test was used to compare the longitudinal data. A *p*-value of 0.05 or below was considered to be significantly different between the groups.

Tissue collection

Animals were euthanized one day after the last MRI session using an overdose of 3 mL/kg pentobarbital sodium (Euthatal, Merial Animal Health Ltd, Harlow, UK) injected intra-peritoneally. An incision was performed along the mid-ventral line through the abdomen to severe the aorta under the diaphragm. A midline thoracotomy gave access to the heart. A 25-gauge needle connected to an extension tube was clamped to the left ventricle of the heart to perfuse with 50 mL saline followed by 75 mL 4% Formalin (Sigma-Aldrich, St. Louis, Massachusetts, USA). Following fixation, brains were collected and suspended in 4% Formalin.

***Ex vivo* MRI**

Ex vivo MR images of the brain suspended in perfluoropolyether oil (Fomblin, Solvay, Brussels, Belgium) were acquired using the same T_2-weighted coronal fast spin echo sequence as the *in vivo* protocol except that 25 averages were used (scan duration = 1 h 12 min). DWI was carried out using the same EPI-DTI sequence that was used *in vivo* with 25 averages (scan duration = 3 h 26 min).

Histology

The brain sample that was used for *ex vivo* DKI study, was embedded in paraffin until sectioning after the DKI study. Hematoxylin and eosin (H&E) staining was performed on 4 μm coronal sections across the tumor. The sections closely matching the *ex vivo* imaging slice was qualitatively analyzed and the extent of cell density and cellular organization was based on visual assessment of staining.

Results

Figure 3 shows representative T_2-weighted MR images of a tumor bearing rat brain, in which the developing tumor could be visualized 8, 11 and 14 days after tumor cells inoculation. All six rats developed tumors in the right cortex, visible on the MRI scans from one week post-surgery. The tumor volume grew from 23.63 ± 10.20 mm^3 (day 8) to 112.40 ± 37.77 mm^3 (day 14). Based on these MRI volumetric measurements, the growth rate was 0.116 $days^{-1}$. The tumor volume doubling-time was 3.65 days (n=6) in agreement with other F98 volumetric studies [26-28].

Figure 2 shows the MD and MK histograms in the tumoral, edematous and contralateral regions of a representative rat and their corresponding maps 14 days post-implantation. A higher MD is observed in the tumor compared to the contralateral cortex, but with overlapping distributions (Figure 2a). The peritumoral edema demonstrated higher MD than both the tumor and the contralateral cortex. The highest MK was observed in the tumoral region, whereas the lowest values were found in the edematous region (Figure 2c). However, the MK voxel distributions from the three regions were overlapping.

The median parametric values of the whole tumor excluding the edema, the peritumoral edema and the contralateral cortex volumes of interest (as shown in Figure 2b) for the six rats are shown as scatter plots in Figure 4 and Figure 5 at day 8, 11 and 14. Table 1 provides the mean and standard deviation values of the diffusivity and kurtosis parameters in the six rats.

Tumors were observed on the MD maps with a concentric hyperintense structure composed of the peritumoral edema and the necrotic core (Figure 2b). The tumor appears hyperintense on the MK maps (Figure 2d). The axial (AD) and radial diffusivity (RD) maps showed a concentric structure similar to that observed on the MD maps formed of high diffusivity in the peritumoral edema and necrotic core. Likewise, the axial kurtosis (AK) maps demonstrated hyperintense tumors. On the other hand, the radial kurtosis (RK) maps did not provide a clear definition of the tumor edges.

Tumor vs. contralateral cortex

A Wilcoxon signed-rank test showed a significantly higher MD in the tumor compared to the contralateral cortex from day 11 ($Z = 2.097$, $p = 0.036$) (Figure 4a). Similar to MD, the RD was significantly higher in the tumor than the contralateral cortex as illustrated in Figure 5b. No significant difference was observed between the tumor AD and the contralateral values (Figure 5a). The fractional anisotropy (FA) was significantly lower in the tumor on day 14 (Figure 5c).

The MK was significantly higher in the tumor compared to the contralateral cortex ($Z = 2.097$, $p = 0.036$ for all time points) (Figure 4b). Median RK was also significantly higher in the tumor compared to the contralateral cortex on day 8 and day 11 (Figure 5e), whereas the tumor AK was not significantly different (Figure 5d). Kurtosis

fractional anisotropy (KFA) was significantly lower in the tumor compared to the contralateral cortex at all time points (Figure 5f).

Tumor vs. peritumoral edema

MD was significantly higher in the edema compared to the tumor and the contralateral cortex from day 8 ($Z = 2.097$, $p = 0.036$) (Figure 4a). RD was also significantly higher in the edema compared to the tumor (Figure 5b), and AD was significantly higher only on day 14 (Figure 5a). FA was significantly greater in the edema compared to the tumor (Figure 5c). MK was significantly lower in the edema compared to the tumor ($Z = 2.097$, $p = 0.036$) (Figure 4b). Significant differences were observed for AK at all time points (Figure 4d), and RK at day 8 and day 11 (Figure 5e). KFA did not show any significant difference between the tumor and the peritumoral edema (Figure 5f).

Longitudinal changes in imaging parameters

The Friedman test showed no significant changes in tumor MD ($\chi^2 = 3,\ df = 2,\ p = 0.22$) or MK ($\chi^2 = 1.33,\ df = 2,\ p = 0.51$) values with time as tumor growth occurred. None of the other diffusivity and kurtosis parameters displayed any significant change with time and tumor growth.

***Ex vivo* diffusivity and kurtosis**

Ex vivo MRI scans and corresponding H&E slices of a representative brain are shown in Figure 6. A reduced FA was observed in the necrotic center of the tumor and in the tumor surroundings (Figure 6a, Table 1). KFA followed the same trend (Figure 6b, Table 1). Comparing the histological section with the similar slice section on MRI, demonstrated a dense tumor (visual appearance of higher staining reflecting

increased cell density) on H&E staining (Figure 6f). The necrotic center was hollow due to the fixation and dehydration processes. The tumor edge seemed to have elevated cellular density compared to the contralateral cortex (Figure 6e).

Discussion

In this study, we investigated the utility of diffusion kurtosis to probe intra-tumoral heterogeneity in a rat model of intracranial glioblastoma. Although diffusion kurtosis demonstrated significant difference between the tumor, the peritumoral edema and the contralateral cortex from the early stage, none of the parameters significantly changed as the tumor grew.

We observed an increased mean diffusivity (MD) and mean kurtosis (MK) in the tumor in comparison with the contralateral cortex. The increased MD may be due to increased extracellular diffusivity, or a significant increase in intracellular water diffusion due to cellular swelling. An increased mean diffusivity in tumors relative to the contralateral cortex has been reported in rats with F98 and C6 glioma [8-10,29], although some discrepancy exists since another study reported decreased MD in C6 gliomas [30]. MRI diffusion parameters, such as MD and FA, have shown potential for predicting tumor grade [31,32], treatment monitoring and prognosis [33]. The F98 tumors exhibited higher MK values compared to the contralateral cortex, similar to some human studies reporting higher MK in high grade tumors compared to lower grade glioma [23,34]. However, higher MK has also been associated with inflammation and glial activity in rat model of traumatic brain injury [19,35]. Hempel et al. [36] reported that MK was a robust parameter for WHO classification of human gliomas. In fact, the highest MK values were measured in IDH_{WT} glioblastoma described by an increased

cellularity, cellular heterogeneity, hemorrhage, necrosis and microvasculature proliferation, and the lowest MK values were observed in IDH_{mut} because of their low cell density and homogeneity [37]. The high MK observed in the F98 glioma in our study might originate from the high cellular density of the tumoral rim and the heterogeneity of the necrotic core, which was verified by H&E staining whereby very high cell density was observed in the tumor, and a slightly increased cell density was observed in the peritumoral area compared to the contralateral cortex.

Radial and axial diffusivities (RD and AD) exhibited the same trend as the MD values in the tumor and the contralateral cortex. Previous studies also reported higher RD in F98, 9L and GBM22 rat tumors [8,10]. We observed that RK was higher in the tumor compared to the contralateral cortex on day 8 and 11 whereas AK was not significantly different between the tumor and the normal brain.

A lower FA value was observed in the tumor compared to the normal brain in our study suggesting a more chaotic cellular organization in the tumor. In an earlier study, higher FA in tumor rim than the tumor core has been reported in the F98 model [9]. As the tumor size increased, the necrotic core grew to become the major part of the tumor VOI by day 14 thereby contributing predominantly to the whole tumor diffusion anisotropy measurements in our study. Similar to our observations, increases in FA have been reported in human tumors from grade II to IV gliomas [31]. Lower KFA from the F98 tumor, especially from the necrotic center indicates a much lower degree of tissue organization. KFA, which represents the anisotropy of the kurtosis tensor, has been recently proposed as useful microstructural contrast [38,39]. Although this metric is more appropriate for white matter analysis in the case of several crossing fiber

orientations in the same voxel, it also seems to be of interest for grey matter microstructure description as elevated KFA was observed in tissues with low anisotropy such as the thalamus and lenticular nucleus where the cells are organized in oriented structures (e.g. lamina, nuclei) [39]. The variability in the normal brain VOI parameters (Figure 5) was larger than expected, especially in the FA, RK and KFA values. The fact that this variability is not observed in all the parameters, suggests that there might be some variability in the selection of the VOI, leading to different GM/WM ratios, and that FA, KFA and RK are probably more sensitive to these subtle alterations than the other DTI and DKI parameters. We observed decreased KFA in the tumoral tissue, suggesting a lower degree of overall tissue organization, which was noted in H&E stains showing high cellular density in the tumor with heterogeneity due to the necrotic cores.

The peritumoral edema displayed higher MD due to increased extracellular water. The increased water diffusion in all directions causes a significant decrease in diffusional kurtosis compared to the contralateral cortex, but also relative to the tumor. Furthermore, the peritumoral edema FA was always significantly higher than that of the tumor. An increased peritumoral edema FA and increased MD were also described in several F98 and 9L rat glioma studies [8-10]. However, an increased FA and decreased ADC (MD) in the area surrounding the tumor was reported by Kim et al. [10] and by Lope-Piedrafita et al. in 9L, F98 and C6 rat glioma, assumed to be caused by the compression of the surrounding cells to an oblate spheroid shape [40]. The increased diffusion anisotropy measured in the peritumoral region can be explained by the compression of the grey matter by the tumor mass, but also the infiltration of the tumor in the surrounding tissue. The H&E staining shows a higher cellular density in the

edematous region. Furthermore, the cells seem to be more elongated in the region directly surrounding the tumor than in the contralateral cortex due to a tumoral mass effect, as suggested by Lope-Piedrafita [40]. It seems that our F98 glioma model is not only highly infiltrative but also demonstrates a mass effect on the nearby tissue.

Diffusion kurtosis imaging (DKI) provides dimensionless metrics on the deviation of the probabilistic water displacement from a Gaussian distribution and has been proposed to better characterize tumor heterogeneity than standard DTI parameters in several pathological conditions (24). In contrast to our hypothesis, we did not observe any temporal evolution in DKI parameters with tumor growth, as the tumor tissue clearly became more heterogenous with time, with increased necrotic areas. An increase of ADC over time has been reported by Letourneur et al. [29] in a rat model with C6 glioma. However, no changes of ADC was observed in in F98 tumors [29] or 9L tumors [41].

Our study did not show any better sensitivity in identifying tumor tissue from healthy brain with DKI, compared to DTI at all imaging time points. Our initial hypothesis was that as the tumor grows, the increased microstructural heterogeneity due to hypoxia and necrosis would be quantifiable using DKI parameters. The lack of significant changes may either be due to tumor biology or due to limitations of the DKI technique. Firstly, the DKI data were acquired at 9.4 T using two non-zero b-values that should theoretically allow kurtosis calculation in our model [38,42], but only two b-values may have not provided enough sensitivity in measuring early microstructural changes, as suggested by other reports which used several low and high b-values combinations [15,17]. The use of the b=0 values for both the DTI and DKI analysis led to some contributions from the fast (vascular) components of water diffusion due to the intra

voxel intra molecular (IVIM) effect. However, since the IVIM effect would have impacted both the DTI and DKI measurements, we believe that the IVIM effects would have cancelled out while comparing the two (DTI versus DKI) for assessing tumor tissue heterogeneity. Additionally, although most human DKI studies are performed using 30 diffusion encoding directions, based on the recommendations of the DKE software, we used 15 diffusion directions in our study as the best compromise between SNR and acquisition time. However, we do not believe that the reduced number of diffusion direction impacts on the DKI fitting as it has been reported that DKI parameters can be calculated using a minimum of 15 diffusion directions [15,16]. Preclinical DKI studies have been reported with 15 directions in a rat model of stroke at 4.7T [43], and 20 directions in diabetic rats at 7T [21]. In fact, Latt et al. demonstrated that even 6 directions are sufficient to reach a good estimate of diffusion kurtosis in human MS at 3T [44]. Another probable reason for not observing any change in kurtosis with tumor growth could be that the tumor was already highly heterogeneous (microstructurally) at the earliest imaging time point. In fact, a necrotic core was observed on the anatomical scans and parametric maps in all of the tumors from day 11 post-implantation (second imaging time point). It is possible that the subsequent changes in tumor heterogeneity were not substantial enough to be detected with diffusion kurtosis MRI. The use of complementary imaging techniques could be useful to assess cellular swelling and extracellular matrix alterations such as time-dependent DTI that was used in tumor models to separate the intracellular and extracellular water diffusion [45,46]. Alternatively, a slower growing tumor model could be used, or a treatment paradigm that substantially alters the tissue microstructure by induction of therapeutic cell death.

Commented [PH1]: R3.1

In conclusion, an increased diffusional kurtosis in F98 tumors, and a decrease in the peritumoral edema was observed compared to the normal brain, although no changes in DKI parameters were noted as the tumor grew, indicating that this technique may not be able to observe the microstructural tumor heterogeneity in the F98 model.

Acknowledgements: Dr Arthur Taylor, University of Liverpool, is acknowledged for providing the F98 cells and the protocol for tumor transplantation. Imaging studies were performed at the Centre for Preclinical Imaging, which was funded in part by a Medical Research Council (MRC) grant (MR/L012707/1).

Figure Legends

Figure 1: Representative T_2-weighted image (a) and its corresponding diffusivity (b) and kurtosis (c) parametric maps. The red arrow indicates the tumor location on the T_2-weighted image.

Figure 2: Mean diffusivity (a) and mean kurtosis (c) histograms in the tumor of a representative rat 14 days after tumor cell injection compared to the contralateral cortex and peritumoral edema and their corresponding mean diffusivity (b) and mean kurtosis (d) maps. The tumor (red), peritumoral edema (green) and contralateral cortex (blue) volumes-of-interest contours are illustrated on the MD (b) and MK (d) maps.

Figure 3: Typical T_2-weighted images of the same rat at a similar slice level showing the presence of F98 tumors (top row, arrow). Boxplots showing the tumor volumes segmented from T_2-weighted images in the six rats 8, 11 and 14 days post-implantation (bottom row).

Figure 4: Comparison boxplots of the median values of mean diffusivity (MD) (a, left) and mean kurtosis (MK) (b, left) in the six rats in the tumor (red), peritumoral edema (yellow) and contralateral cortex (blue) (*: $p<0.05$), and representative MD and MK maps at day 8, day 11 and day 14 (right).

Figure 5: Boxplots of the axial diffusivity (a), radial diffusivity (b), fractional anisotropy (c), axial kurtosis (d), radial kurtosis (e) and kurtosis fractional anisotropy (f) in the

tumor, the contralateral healthy cortex and the edema, day 8, 11 and 14 post-implantation (*: $p<0.05$).

Figure 6: FA (a) and KFA (b) maps of an *ex vivo* rat brain and corresponding 10X H&E staining (c). 20X magnification on the edematous region (d), the tumor edge (e), the tumor center (f) and the contralateral cortex (g). The red arrows indicate the tumor on the FA and KFA maps.

References

1. Hanif F, Muzaffar K, Perveen K, Malhi SM, Simjee SU. Glioblastoma Multiforme: A Review of its Epidemiology and Pathogenesis through Clinical Presentation and Treatment. *Asian Pacific Journal of Cancer Prevention : APJCP.* 2017;18(1):3-9.
2. Barth RF, Kaur B. Rat brain tumor models in experimental neuro-oncology: the C6, 9L, T9, RG2, F98, BT4C, RT-2 and CNS-1 gliomas. *Journal of Neuro-Oncology.* 2009;94(3):299-312.
3. Ortensi B, Setti M, Osti D, Pelicci G. Cancer stem cell contribution to glioblastoma invasiveness. *Stem Cell Research & Therapy.* 2013;4(1):18.
4. Coquery N, Serduc R, Rémy C, Barbier EL, Lemasson B. Cluster versus ROI analysis to assess combined antiangiogenic therapy and radiotherapy in the F98 rat-glioma model. *NMR in Biomedicine.* 2018;31(8):e3933.
5. Côté J, Savard M, Bovenzi V, et al. Selective tumor blood–brain barrier opening with the kinin B2 receptor agonist [Phe8ψ(CH2NH)Arg9]-BK in a F98 glioma rat model: An MRI study. *Neuropeptides.* 2010;44(2):177-185.
6. Bolcaen J, Descamps B, Acou M, et al. In Vivo DCE-MRI for the Discrimination Between Glioblastoma and Radiation Necrosis in Rats. *Molecular Imaging and Biology.* 2017;19(6):857-866.
7. Coquery N, Stupar V, Farion R, et al. The three glioma rat models C6, F98 and RG2 exhibit different metabolic profiles: in vivo 1H MRS and ex vivo 1H HRMAS combined with multivariate statistics. *Metabolomics.* 2015;11(6):1834-1847.
8. Wang S, Zhou J. Diffusion tensor MR imaging of rat glioma models: A correlation study of MR imaging and histology. *Journal of computer assisted tomography.* 2012;36(6):739-744.

9. Zhang J, van Zijl PCM, Laterra J, et al. Unique Patterns of Diffusion Directionality in Rat Brain Tumors Revealed by High-Resolution Diffusion Tensor MRI. *Magnetic resonance in medicine : official journal of the Society of Magnetic Resonance in Medicine / Society of Magnetic Resonance in Medicine.* 2007;58(3):454-462.

10. Kim S, Pickup S, Hsu O, Poptani H. Diffusion tensor MRI in rat models of invasive and well-demarcated brain tumors. *NMR in Biomedicine.* 2007;21(3):208-216.

11. Engelhorn T, Schwarz MA, Hess A, et al. Definition of Ktrans and FA Thresholds for Better Assessment of Experimental Glioma Using High-field MRI: A Feasibility Study. *Clinical Neuroradiology.* 2014;24(4):337-345.

12. Le Bihan D, Breton E, Lallemand D, Aubin ML, Vignaud J, Laval-Jeantet M. Separation of diffusion and perfusion in intravoxel incoherent motion MR imaging. *Radiology.* 1988;168(2):497-505.

13. Le Bihan D, Breton E, Lallemand D, Grenier P, Cabanis E, Laval-Jeantet M. MR imaging of intravoxel incoherent motions: application to diffusion and perfusion in neurologic disorders. *Radiology.* 1986;161(2):401-407.

14. Stejskal EO, Tanner JE. Spin Diffusion Measurements: Spin Echoes in the Presence of a Time-Dependent Field Gradient. *The Journal of Chemical Physics.* 1965;42(1):288-292.

15. Jensen JH, Helpern JA. MRI quantification of non-Gaussian water diffusion by kurtosis analysis. *NMR in Biomedicine.* 2010;23(7):698-710.

16. Jensen JH, Helpern JA, Ramani A, Lu H, Kaczynski K. Diffusional kurtosis imaging: The quantification of non-gaussian water diffusion by means of

magnetic resonance imaging. *Magnetic Resonance in Medicine.* 2005;53(6):1432-1440.

17. Fieremans E, Jensen JH, Helpern JA. White matter characterization with diffusional kurtosis imaging. *NeuroImage.* 2011;58(1):177-188.
18. Umesh Rudrapatna S, Wieloch T, Beirup K, et al. Can diffusion kurtosis imaging improve the sensitivity and specificity of detecting microstructural alterations in brain tissue chronically after experimental stroke? Comparisons with diffusion tensor imaging and histology. *NeuroImage.* 2014;97:363-373.
19. Braeckman K, Descamps B, Pieters L, Vral A, Caeyenberghs K, Vanhove C. Dynamic changes in hippocampal diffusion and kurtosis metrics following experimental mTBI correlate with glial reactivity. *NeuroImage: Clinical.* 2019;21:101669.
20. Vanhoutte G, Pereson S, Delgado y Palacios R, et al. Diffusion kurtosis imaging to detect amyloidosis in an APP/PS1 mouse model for Alzheimer's disease. *Magnetic Resonance in Medicine.* 2013;69(4):1115-1121.
21. Ding G, Chen J, Chopp M, et al. White matter changes after stroke in type 2 diabetic rats measured by diffusion magnetic resonance imaging. *Journal of Cerebral Blood Flow & Metabolism.* 2015;37(1):241-251.
22. Chen X-r, Zeng J-y, Shen Z-W, Kong L-m, Zheng W-b. Diffusion Kurtosis Imaging Detects Microstructural Changes in the Brain after Acute Alcohol Intoxication in Rats. *BioMed Research International.* 2017;2017:6.
23. Hempel JM, Schittenhelm J, Bisdas S, et al. In vivo assessment of tumor heterogeneity in WHO 2016 glioma grades using diffusion kurtosis imaging: Diagnostic performance and improvement of feasibility in routine clinical practice. *Journal of Neuroradiology.* 2018;45(1):32-40.

24. Liu H, Shen W, Zhang C, et al. Diffusion kurtosis imaging evaluating epithelial–mesenchymal transition in colorectal carcinoma xenografts model: a preliminary study. *Scientific Reports.* 2017;7(1):11424.

25. Talkington A, Durrett R. Estimating Tumor Growth Rates In Vivo. *Bulletin of mathematical biology.* 2015;77(10):1934-1954.

26. Mathieu D, Lecomte R, Tsanaclis AM, Larouche A, Fortin D. Standardization and Detailed Characterization of the Syngeneic Fischer/F98 Glioma Model. *Canadian Journal of Neurological Sciences / Journal Canadien des Sciences Neurologiques.* 2007;34(3):296-306.

27. Doblas S, He T, Saunders D, et al. Glioma morphology and tumor-induced vascular alterations revealed in seven rodent glioma models by in vivo magnetic resonance imaging and angiography. 2010;32(2):267-275.

28. Yang W, Barth RF, Wu G, et al. Development of a Syngeneic Rat Brain Tumor Model Expressing EGFRvIII and Its Use for Molecular Targeting Studies with Monoclonal Antibody L8A4. 2005;11(1):341-350.

29. Letourneur A, Roussel S, Bernaudin M, et al. Chronic arterial hypertension impedes glioma growth: a multiparametric MRI study in the rat. *Hypertension Research.* 2015;38:723.

30. Bennett KM, Hyde JS, Rand SD, et al. Intravoxel distribution of DWI decay rates reveals C6 glioma invasion in rat brain. *Magnetic Resonance in Medicine.* 2004;52(5):994-1004.

31. Inoue T, Ogasawara K, Beppu T, Ogawa A, Kabasawa H. Diffusion tensor imaging for preoperative evaluation of tumor grade in gliomas. *Clinical Neurology and Neurosurgery.* 2005;107(3):174-180.

32. Leu K, Ott GA, Lai A, et al. Perfusion and diffusion MRI signatures in histologic and genetic subtypes of WHO grade II–III diffuse gliomas. *Journal of Neuro-Oncology.* 2017;134(1):177-188.

33. Ellingson BM, Gerstner ER, Smits M, et al. Diffusion MRI Phenotypes Predict Overall Survival Benefit from Anti-VEGF Monotherapy in Recurrent Glioblastoma: Converging Evidence from Phase II Trials. *Clinical Cancer Research.* 2017;23(19):5745.

34. Van Cauter S, Veraart J, Sijbers J, et al. Gliomas: Diffusion Kurtosis MR Imaging in Grading. *Radiology.* 2012;263(2):492-501.

35. Zhuo J, Xu S, Proctor JL, et al. Diffusion kurtosis as an in vivo imaging marker for reactive astrogliosis in traumatic brain injury. *NeuroImage.* 2012;59(1):467-477.

36. Hempel J-M, Schittenhelm J, Brendle C, et al. Histogram analysis of diffusion kurtosis imaging estimates for in vivo assessment of 2016 WHO glioma grades: A cross-sectional observational study. *European Journal of Radiology.* 2017;95:202-211.

37. Hempel J-M, Bisdas S, Schittenhelm J, et al. In vivo molecular profiling of human glioma using diffusion kurtosis imaging. *Journal of Neuro-Oncology.* 2017;131(1):93-101.

38. Hansen B, Jespersen SN. Kurtosis fractional anisotropy, its contrast and estimation by proxy. *Scientific Reports.* 2016;6:23999.

39. Glenn GR, Helpern JA, Tabesh A, Jensen JH. Quantitative assessment of diffusional kurtosis anisotropy. *NMR in Biomedicine.* 2015;28(4):448-459.

40. Lope-Piedrafita S, Garcia-Martin ML, Galons J-P, Gillies RJ, Trouard TP. Longitudinal diffusion tensor imaging in a rat brain glioma model. *NMR in Biomedicine.* 2008;21(8):799-808.

41. Kopelman R, Lee Koo Y-E, Philbert M, et al. Multifunctional nanoparticle platforms for in vivo MRI enhancement and photodynamic therapy of a rat brain cancer. *Journal of Magnetism and Magnetic Materials.* 2005;293(1):404-410.

42. Yan X, Zhou M, Ying L, et al. Evaluation of optimized b-value sampling schemas for diffusion kurtosis imaging with an application to stroke patient data. *Computerized Medical Imaging and Graphics.* 2013;37(4):272-280.

43. Sun PZ, Wang Y, Mandeville E, Chan S-T, Lo EH, Ji X. Validation of fast diffusion kurtosis MRI for imaging acute ischemia in a rodent model of stroke. *NMR in Biomedicine.* 2014;27(11):1413-1418.

44. Lätt J, Nilsson M, Wirestam R, et al. In vivo visualization of displacement-distribution-derived parameters in q-space imaging. *Magnetic Resonance Imaging.* 2008;26(1):77-87.

45. Reynaud O, Winters KV, Hoang DM, Wadghiri YZ, Novikov DS, Kim SG. Surface-to-volume ratio mapping of tumor microstructure using oscillating gradient diffusion weighted imaging. *Magnetic Resonance in Medicine.* 2016;76(1):237-247.

46. Hope TR, White NS, Kuperman J, et al. Demonstration of Non-Gaussian Restricted Diffusion in Tumor Cells Using Diffusion Time-Dependent Diffusion-Weighted Magnetic Resonance Imaging Contrast. *Frontiers in Oncology.* 2016;6(179).

Table 1: Mean ± standard deviation for all diffusion and kurtosis parameters in the tumor, edema and contralateral cortex volumes-of-interest of the six rats. (**#**: significant difference between the tumor and the contralateral cortex, **$**: significant difference between the tumor and the edema). Mean and standard deviation from the *ex vivo* data were taken from the volume of interest in one representative rat.

		MD x 10^{-3} (μm^2/ms)	AD x 10^{-3} (μm^2/ms)	RD x 10^{-3} (μm^2/ms)	FA	MK	AK	RK	KFA
Day 8	Tumor	0.78±0.04	0.90±0.06	0.71±0.04	0.16±0.04	0.87±0.05	0.89±0.07	0.86±0.09	0.49±0.15
	Edema	0.87±0.06 $	1.03±0.08	0.79±0.06 $	0.19±0.02	0.76±0.03 $	0.78±0.06 $	0.75±0.05 $	0.50±0.16
	Contralateral cortex	0.71±0.03	0.84±0.03 #	0.64±0.03 #	0.17±0.03	0.78±0.09 #	0.75±0.26	0.70±0.17 #	0.60±0.18 #
Day 11	Tumor	0.75±0.04	0.86±0.05	0.70±0.03	0.15±0.03	0.84±0.06	0.91±0.79	0.79±0.11	0.47±0.10
	Edema	0.88±0.03 $	1.03±0.08	0.79±0.03 $	0.22±0.02 $	0.74±0.04 $	0.79±0.03 $	0.71±0.08 $	0.50±0.09
	Contralateral cortex	0.68±0.04 #	0.78±0.04	0.61±0.04 #	0.19±0.05	0.75±0.07 #	0.92±0.02	0.67±0.12 #	0.62±0.11 #
Day 14	Tumor	0.74±0.05	0.83±0.03	0.67±0.02	0.14±0.03	0.82±0.08	0.88±0.06	0.77±0.08	0.49±0.06
	Edema	0.89±0.04 $	1.07±0.05 $	0.80±0.04 $	0.22±0.02 $	0.73±0.02 $	0.74±0.04 $	0.72±0.06	0.46±0.06
	Contralateral cortex	0.67±0.01 #	0.82±0.03	0.59±0.01 #	0.22±0.02 #	0.72±0.06 #	0.83±0.06	0.73±0.11	0.62±0.05 #
Ex vivo	Tumor	0.55±0.08	0.63±0.08	0.51±0.08	0.18±0.07	0.90±0.15	0.86±0.14	0.83±0.18	0.42±0.08
	Contralateral cortex	0.31±0.01	0.37±0.02	0.28±0.01	0.23±0.03	1.65±0.12	1.61±0.17	1.56±0.16	0.50±0.05

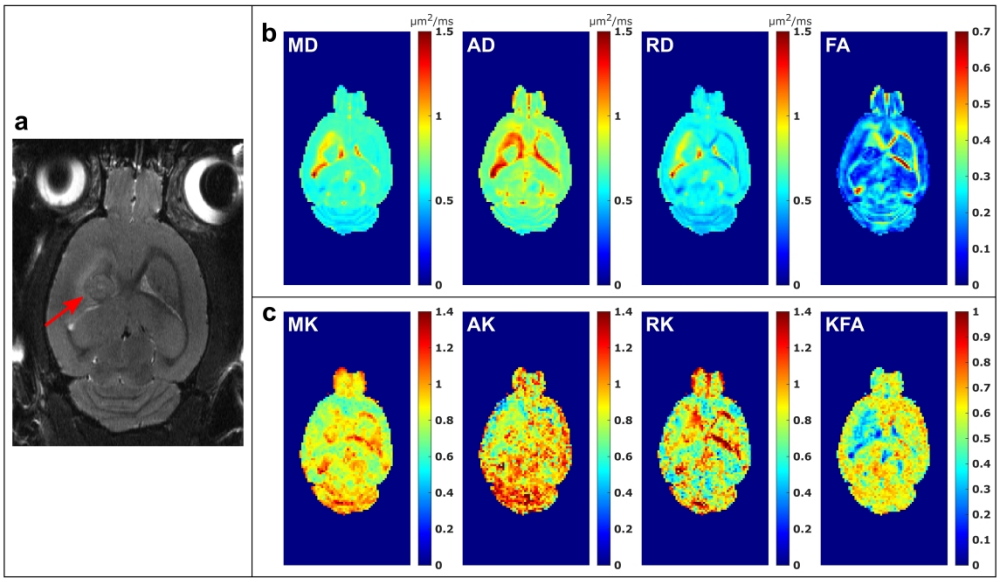

Figure 1: Representative T2-weighted image (a) and its corresponding diffusivity (b) and kurtosis (c) parametric maps. The red arrow indicates the tumor location on the T2-weighted image.

1890x1132mm (96 x 96 DPI)

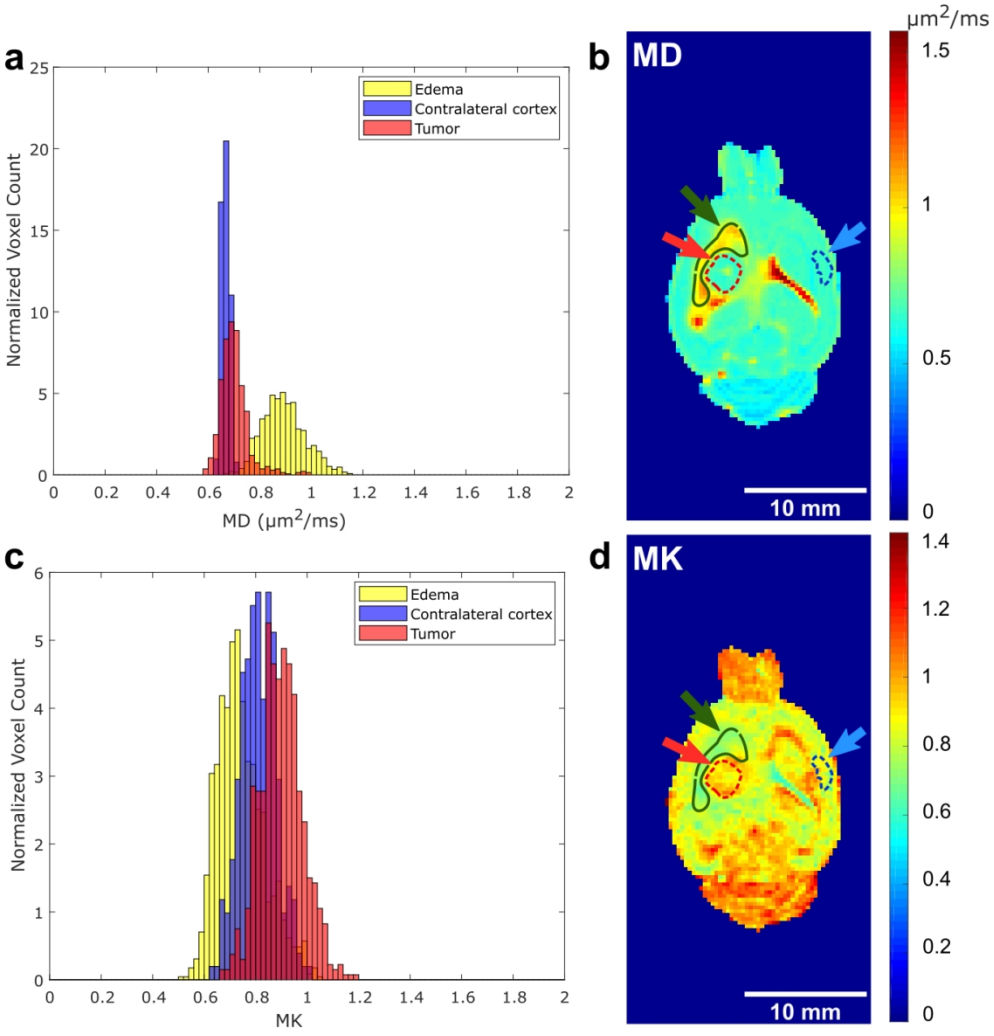

Figure 2: Mean diffusivity (a) and mean kurtosis (c) histograms in the tumor of a representative rat 14 days after tumor cell injection compared to the contralateral cortex and peritumoral edema and their corresponding mean diffusivity (b) and mean kurtosis (d) maps. The tumor (red), peritumoral edema (green) and contralateral cortex (blue) volumes-of-interest contours are illustrated on the MD (b) and MK (d) maps.

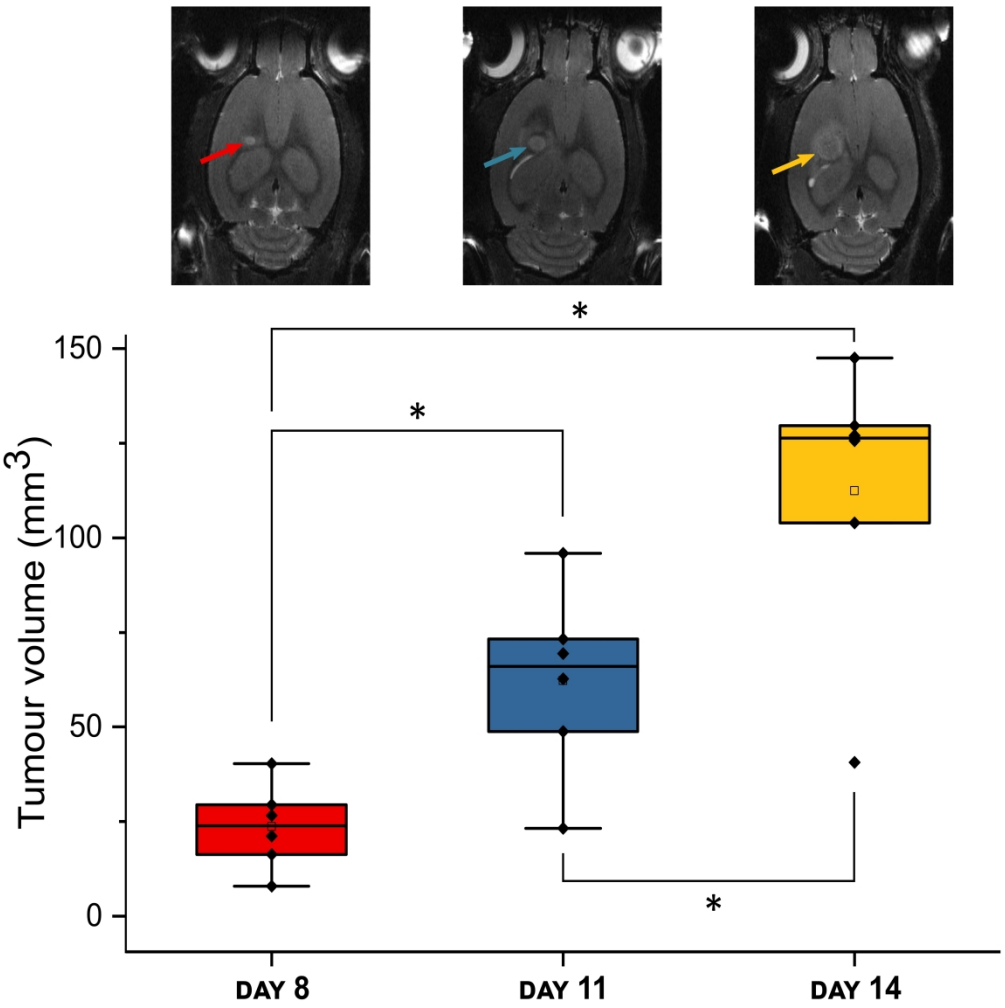

Figure 3: Typical T2-weighted images of the same rat at a similar slice level showing the presence of F98 tumors (top row, arrow). Boxplots showing the tumor volumes segmented from T2-weighted images in the six rats 8, 11 and 14 days post-implantation (bottom row).

1763x1763mm (72 x 72 DPI)

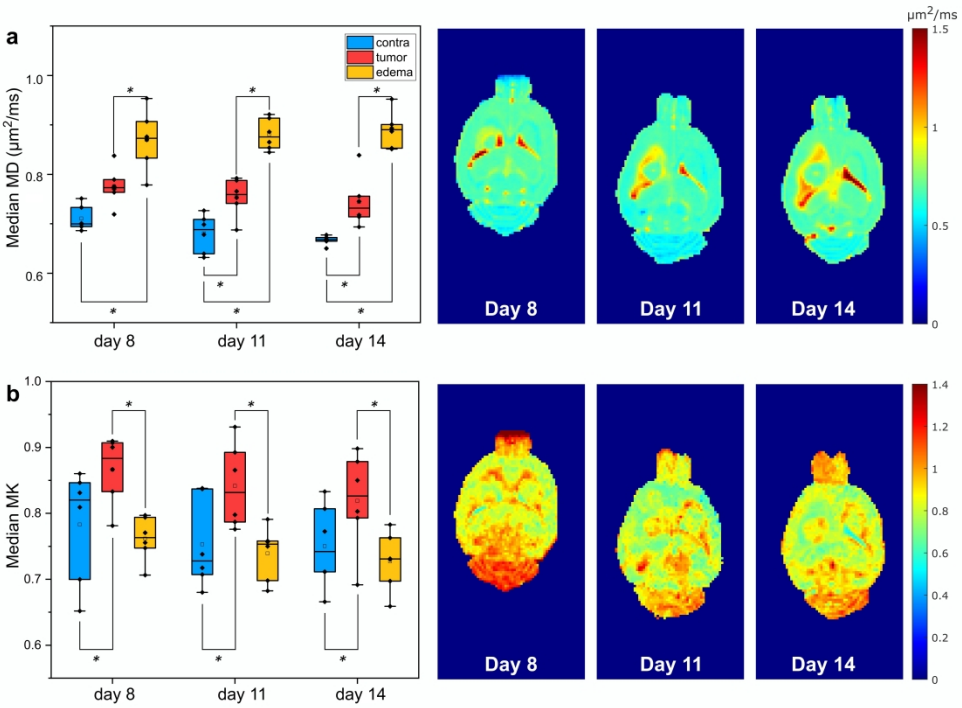

Figure 4: Comparison boxplots of the median values of mean diffusivity (MD) (a, left) and mean kurtosis (MK) (b, left) in the six rats in the tumor (red), peritumoral edema (yellow) and contralateral cortex (blue) (*: $p<0.05$), and representative MD and MK maps at day 8, day 11 and day 14 (right).

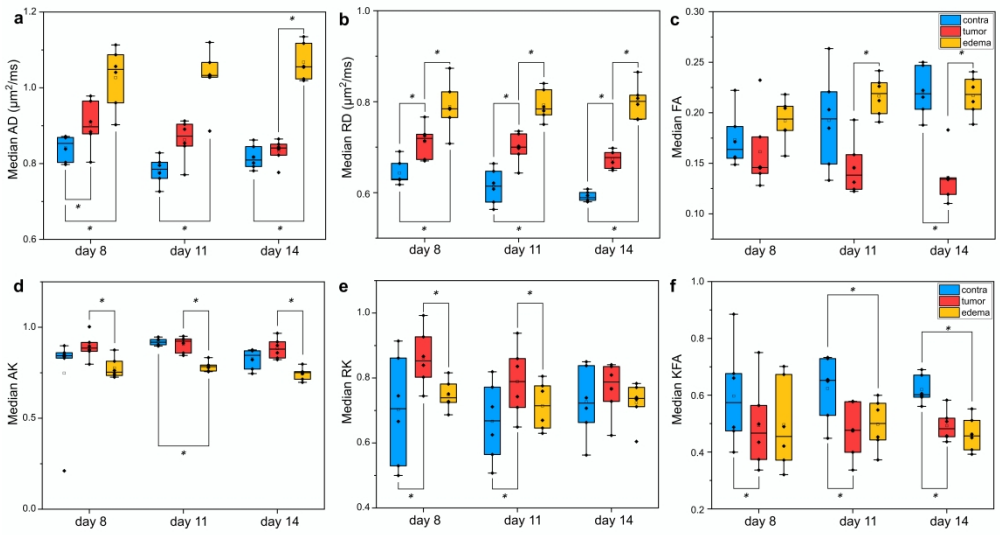

Figure 5: Boxplots of the axial diffusivity (a), radial diffusivity (b), fractional anisotropy (c), axial kurtosis (d), radial kurtosis (e) and kurtosis fractional anisotropy (f) in the tumor, the contralateral healthy cortex and the edema, day 8, 11 and 14 post-implantation (*: $p<0.05$).

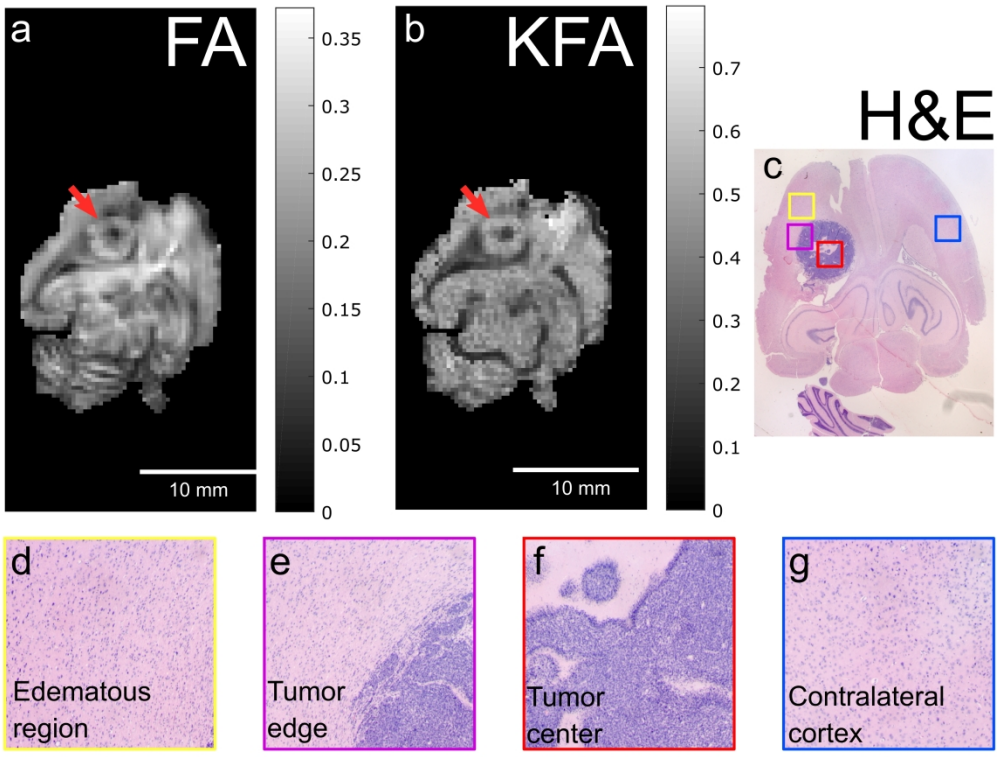

Figure 6: FA (a) and KFA (b) maps of an ex vivo rat brain and corresponding 10X H&E staining (c). 20X magnification on the edematous region (d), the tumor edge (e), the tumor center (f) and the contralateral cortex (g). The red arrows indicate the tumor on the FA and KFA maps.

Diffusion kurtosis imaging for characterization of tumor heterogeneity in an intracranial rat glioblastoma model

Clémentine Lesbats, Claire Louise Kelly, Gabriela Czanner, Harish Poptani*

Diffusion kurtosis imaging (DKI) was performed longitudinally in a rat model of glioblastoma to assess intra-tumor heterogeneity. Although mean kurtosis values were significantly higher in the tumor compared to the healthy brain cortex or peri-tumoral edema, no significant changes in any of the DKI parameters of the tumor were observed when the values were compared longitudinally.